



Research paper

Non-precious metal electrocatalysts for hydrogen production in proton exchange membrane water electrolyzer



Hoyoung Kim^a, Eunkyoung Hwang^a, Hyunjoo Park^a, Byung-Seok Lee^b, Jong Hyun Jang^b, Hyoung-Juhn Kim^b, Sang Hyun Ahn^{c,*}, Soo-Kil Kim^{a,*}

^a School of Integrative Engineering, Chung-Ang University, 84 Heukseok-ro, Dongjak-gu, Seoul, 06974, Republic of Korea

^b Fuel Cell Research Center, Korea Institute of Science and Technology (KIST), 14-gil 5 Hwarangno, Seongbuk-gu, Seoul, 02792, Republic of Korea

^c School of Chemical Engineering and Material Science, Chung-Ang University, 84 Heukseok-ro, Dongjak-gu, Seoul, 06974, Republic of Korea

ARTICLE INFO

Article history:

Received 8 August 2016

Received in revised form

13 November 2016

Accepted 25 January 2017

Available online 29 January 2017

ABSTRACT

Electrodeposited Cu_xMo_{100-x} catalysts were prepared on a Ti substrate for the hydrogen evolution reaction (HER) in acidic medium. By varying the electrolyte composition for electrodeposition, the atomic concentration of the Cu_xMo_{100-x} electrocatalysts could be controlled, and the Mo content ranged between 0.8 and 6.9%. In the first cyclic voltammetry scan in a 0.5 M H₂SO₄ electrolyte, the recorded HER current densities of the Cu_xMo_{100-x} electrocatalysts at -0.50 V_{RHE} increased on increasing the Mo content to 3.8%; then, a further increase in Mo to 6.9% led to a saturation in the HER activity. The maximum value of the normalized current density with respect to the electrochemical surface area and the loading mass was found for the Cu_{99.2}Mo_{0.8} electrocatalyst. Characterization of the prepared catalysts revealed that the enhancement of catalytic activity originates from changes in the grain size and electronic structure. To operate a single cell of the proton exchange membrane water electrolyzer (PEMWE), we electrodeposited CuMo catalyst on carbon paper, and this was used as the cathode, while IrO₂ electrodeposited on carbon paper was used as the anode. The cell performance was normalized with respect to the metal mass loading and was found to be 3.4 A/mg_{metal} at 1.9 V, a 2.2–10.8 times better catalyst cost-activity relationship compared to that of currently reported PEMWEs using Pt-based cathodes. Consequently, the results presented here show that non-noble metal cathodes can be used for PEMWE operation.

© 2017 Elsevier B.V. All rights reserved.

1. Introduction

Hydrogen is a clean and efficient fuel with various applications in electrochemical energy conversion, especially in fuel cells for vehicle and power generation [1,2]. Water electrolysis is one means of producing pure hydrogen, and electrolysis powered by electricity generated from renewable sources (e.g., sunlight, wind, etc.) is environmentally friendly [3,4]. Recent investigations have used solid polymer electrolyte water electrolyzers (SPEWEs), which have many advantages over alkaline diaphragm water electrolyzers, for example, simple construction/maintenance, generation of high purity hydrogen, low ohmic resistance, and prevention of gas crossover [5]. There are two types of SPEWEs, and these are classified by the type of conducting ions in the solid polymer electrolytes: proton exchange membrane water electrolyzer (PEMWE) [6–11] and anion exchange membrane water electrolyzer

(AEMWE) [12–17]. However, PEMWEs are more efficient and produce more hydrogen faster than AEMWEs [6–17].

Nevertheless, practical applications of PEMWEs have been limited by their high cost, which arises in part owing to their use of large amounts of noble metals [6,18]. In addition, the oxygen evolution reaction (OER) at the anode is known to be a kinetic bottleneck [19–22], and noble metals and their oxide catalysts for OER (e.g., RuO₂ and IrO₂) undergo severe corrosion under acidic conditions when operating at highly positive overpotentials [23–25]. These disadvantages have led to extensive research into the development of noble metal alloy OER catalysts [26,27] or noble metals overlaid [28,29] with other elements to obtain reasonable activity and stability. Concerning the cathodic reactions, Pt metal is the best HER catalyst [30,31], although platinum group metals (PGMs) are also highly active and stable catalysts for acidic HER [32]. Consequently, modified PGM catalysts have been heavily investigated over the last few decades [33]. During operation of PEMWEs, HER catalysts suffer fewer kinetic and stability problems because of the relatively facile reduction of protons in acidic media and the negative poten-

* Corresponding authors.

E-mail address: shahn@cau.ac.kr (S.H. Ahn).

tial window for operation, respectively. This opens the possibility of using non-noble metals as HER catalysts for PEMWE.

For many years, HER electrocatalysis on various metals has been investigated theoretically and experimentally [33–37]. Using density functional theory and electrochemical measurements, Nørskov et al. demonstrated that there are strong correlations between the hydrogen binding energy and HER activity for various PGMs and non-noble metals [37]. The calculated free energy of hydrogen adsorption (ΔG_H) on PGMs (e.g., Pt, Pd, Rh, and Ir) range from –1.4 to 0.02 eV, and the HER exchange current densities range from $10^{-3.7}$ to $10^{-3.0}$ A/cm² [37]. The HER exchange current densities of non-noble metals (e.g., Ni, Co, Cu and W) are 2–3 orders lower than those of PGMs and have ΔG_H values far from zero [37]. Despite their low activities for acidic HER, non-noble metals are still attractive catalysts because of their low cost.

Consequently, various non-noble metals have been studied for acidic HER; [19] in particular, Ni is known to be an effective HER catalyst [30]. Strategies to increase the activity and stability of non-noble metal catalysts have mainly focused on the alloying or overlaying of other elements to improve electronic effects and increase the electrochemically active surface area (ECSA) [38–52]. However, Ni and Ni-based catalysts (e.g., Ni metal alloy, NiS_x, NiP_x, etc.) can undergo dissolution during HER because the standard reduction potential of Ni ($\text{Ni}^{2+} + 2\text{e}^- \rightarrow \text{Ni}$) is –0.280 V vs. the normal hydrogen electrode (NHE); [53] furthermore, this problem also limits the acidic HER catalysis on other non-noble metals such as Co (–0.277 V_{NHE}), Fe (–0.440 V_{NHE}), and Mo (–0.200 V_{NHE}) [53]. Regarding the standard reduction potential, Cu (0.339 V_{NHE}) is an attractive non-noble metal for stable HER catalyst in an acidic environment [53]. However, Cu catalysts have not been significantly studied because Cu is not highly active for the acidic HER, as has been shown by theoretical and experimental investigations [35–37].

In this study, we prepared and characterized nanocrystalline Cu_xMo_{100-x} catalysts for acidic HER and found that they have high catalytic activity for HER catalysis. The nanocrystalline Cu_xMo_{100-x} catalysts were prepared by electrodeposition. The morphologies were observed by field emission scanning electron microscope (FESEM) and compositional analysis was conducted by energy dispersive spectroscopy (EDS). The crystal and electronic structures were characterized by X-ray diffraction (XRD) and X-ray photoelectron spectroscopy (XPS), respectively. The catalytic activities were examined by repeated cyclic voltammetry (CV) in H₂SO₄ electrolyte. Furthermore, the performance of PEMWE single cells using the developed CuMo HER catalysts as the cathode were examined and their performance was discussed. We would like to emphasize that PEMWE operation with a non-noble metal cathode is not common.

2. Experimental

Electrodeposition was used to prepare the Cu_xMo_{100-x} catalysts, and a conventional three-electrode cell was used. For electrodeposition, Ti foil (Sejin, 2 × 2 cm², thickness: 0.1 mm) was used as a working electrode and sealed by a home-made Teflon holder with an area exposed to the electrolyte of 1.13 cm². A Pt wire and saturated calomel electrode (SCE) were employed as counter and reference electrodes, respectively. Prior to electrodeposition, the organic residues on the Ti foil surface were removed by sonication in a 20% ethanol solution for 10 min. Then, the native oxide on the Ti foil surface was eliminated by using a 6 M HCl solution at 70 °C for 30 min [27].

To prepare the electrolyte, 0.05 M CuSO₄·7H₂O (Daejung, 2588–4400) and 0.25 M Na₃C₆H₅O₇ (Sigma-Aldrich, C3474) were

dissolved in 18.2 MΩ deionized water; then, Na₂MoO₄·2H₂O (Sigma-Aldrich, 331058) was added to the electrolyte at

concentrations from 0.01 to 0.60 M. The prepared electrolytes were purged by N₂ bubbling for 30 min. The electrodeposition was carried out at constant potential (–1.0 V_{SCE} for 600 s), controlled by a potentiostat (Autolab, PGSTAT302F, Metrohm). All experimental conditions for electrodeposition are summarized in the Supporting Information (Table S1).

To characterize the electrodeposited Cu_xMo_{100-x} catalysts, we used several analytical techniques. Morphological and compositional observation of the electrodeposits were conducted by FESEM (Sigma, Carl Zeiss) and EDS (Thermo, Noran System 7), respectively. The crystal structures and grain size were analyzed by XRD (New D-8 Advance, Bruker-AXS) with the rate of 5°/min in the range of 30–80°. The change of electronic structure after addition of Mo to Cu was investigated by XPS (Kratos, AXIS-His). The ECSA was measured by linear sweep voltammetry (LSV) with the potential range of –1.2 to 0.5 V_{SCE} at a scan rate of 10 mV/s in 0.5 M NaOH electrolyte [54,55].

The catalytic activities and stabilities of the electrodeposited Cu_xMo_{100-x} catalysts were examined by repeated CV scans within the potential range of –0.2 to –0.8 V_{SCE} at a scan rate of 50 mV/s in 0.5 M H₂SO₄ electrolyte under atmospheric conditions. Two types of electrochemical cells such as a non-divided batch cell and an H-type cell with Nafion membrane to divide the cathodic and anodic parts were used; the non-divided batch cell was used in the initial activity test while both cells were used in the stability test to confirm the effect of dissolution of Pt anode during the repeated cycles. The pH of the 0.5 M H₂SO₄ electrolyte was measured by pH meter (UB-7, Denver Instrument), and all potentials are expressed with respect to the reversible hydrogen electrode (RHE). Electrochemical impedance spectroscopy (EIS, Iviumstat, Ivium Technology) was used to determine the electrolyte resistance between the working and reference electrodes at constant potential of –0.4 V_{SCE} and a frequency scan of 10^{–2}–10⁵ Hz. The averages of electrolyte resistances for the non-divided batch cell and the H-type cell were 1.79 ± 0.03 and 0.93 ± 0.01 Ω, respectively. The obtained values were used for iR-correction of the voltammetry results.

To prepare a PEMWE single cell test, we electrodeposited Cu_{93.7}Mo_{6.3} and IrO₂ catalysts onto carbon paper (CP, TGPH-090, Toray) for use as cathode and anode, respectively. The membrane electrode assembly (MEA) was fabricated by sandwiching the IrO₂/CP anode [7] and Cu_{93.7}Mo_{6.3}/CP cathodes on both sides of the Nafion membrane (212, Dupont Co.). The active area of the MEA was 4 cm². After cell assembly, the temperature of the cell was maintained at 90 °C. Pre-heated deionized water (50 °C) was injected into the PEMWE as a reactant with a flow rate of 15 mL/min. For single-cell operation, the potentiostatic method was adopted with the potential window from 1.35 to 2.00 V_{cell}, and the stabilized currents after 5 min for each potential were recorded with an interval of 0.05 V.

3. Results and discussion

Fig. 1 shows the morphologies of Cu₁₀₀ and Cu_xMo_{100-x} deposits and their elemental compositions obtained by EDS analysis (see Fig. S1 in Supporting Information). The Cu₁₀₀ deposit contains polygonal aggregates with sizes ranging from 100 to 200 nm (**Fig. 1a**). When the Mo content of the alloy was 0.8%, the size of the aggregates relative to those of pure copper changed little; however, the angles between the faces of the aggregates became sharper and the surfaces rougher (**Fig. 1b**). On increasing the Mo content to 2.4%, the morphology drastically changed, becoming dendritic with sharp edges (**Fig. 1c**). On increasing the Mo content from 3.8 to 6.9%, the particles became more rounded (**Fig. 1d–f**). The

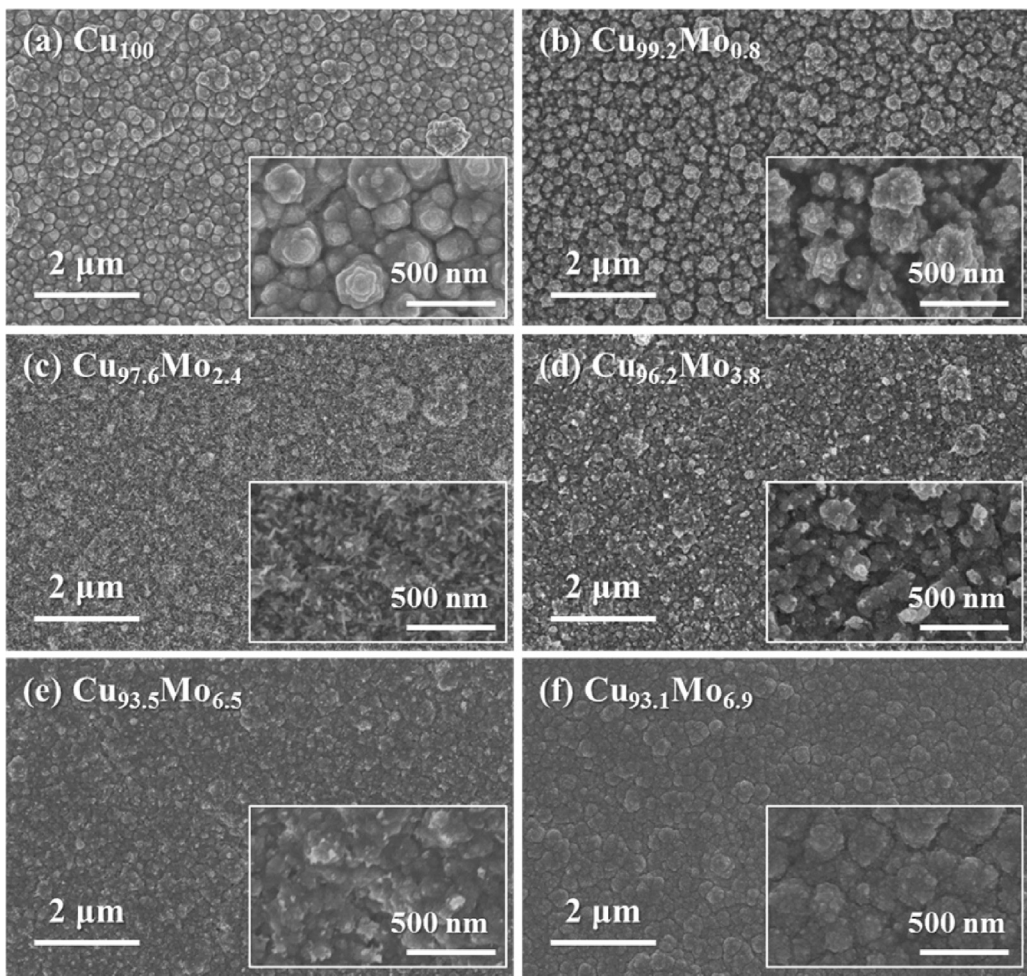


Fig. 1. FESEM images of Cu_{100} and $\text{Cu}_x\text{Mo}_{100-x}$ deposits. The inset images show details at high magnifications.

aggregates of the $\text{Cu}_{93.1}\text{Mo}_{6.9}$ deposit showed slightly larger sizes compared those of the Cu_{100} deposit. In addition, element mapping analysis confirmed that the Cu and Mo were well distributed on the selected area (see Fig. S2 in Supporting Information).

The crystal structures of the Cu_{100} and $\text{Cu}_x\text{Mo}_{100-x}$ deposits were examined by XRD analysis, as presented in Fig. 2a. As a reference, the XRD patterns of the Ti foil substrates are shown as a gray line, and these patterns are well matched to that of Ti (JCPDS #44-1294) [27]. For the Cu_{100} deposit, peaks were observed at 43.30 and 50.43°, reflections characteristic of the (111) and (200) faces of copper, respectively. However, as the Mo content of the alloy increased, the intensity of the Cu(111) peaks decreased significantly, and the peaks became broader compared to those of the Cu_{100} deposit. Furthermore, the Cu(200) peaks of the $\text{Cu}_x\text{Mo}_{100-x}$ deposits were insignificant. The full-width half-maximum (FWHM) of the Cu(111) peaks increased with increasing Mo content, and the values were used to calculate the grain size of the deposit using the Scherrer equation, as shown in Fig. 2b. The calculated grain size of the pure copper deposit was about 34 nm, based on the (111) reflection, and the particle size rapidly decreased on adding Mo (13.0–19.1 nm).

To calculate the mass metal loading after electrodeposition, we immersed the Cu and $\text{Cu}_x\text{Mo}_{100-x}$ deposits in 0.5 M H_2SO_4 , and a constant potential of 0.5 V_{SCE} was immediately applied for 60 s to dissolve completely the electrodeposits. As a reference, the stability of the pretreated Ti foil substrate was also tested under the same conditions. The results of chronoamperometry are shown in Fig. 2c. The dissolution current of the Ti foil substrate was negligible, indicating that the recorded currents for the $\text{Cu}_x\text{Mo}_{100-x}$

deposits were completely used in their dissolution. The calculated charge density of Cu and $\text{Cu}_x\text{Mo}_{100-x}$ deposits are plotted and shown in Fig. 2d. The Cu deposit has a dissolution charge density of about 900 mC/cm_{geo}², and the charge density of the $\text{Cu}_x\text{Mo}_{100-x}$ deposits was larger than that of Cu deposit, except in the case of the $\text{Cu}_{99.2}\text{Mo}_{0.8}$ deposit. The mass loadings of Cu and Mo were then calculated, based on the charges and the composition obtained by EDS analysis. All mass loadings were found to be on the scale of sub-milligrams per square centimeter. The calculated loading mass of Cu_{100} deposit was 0.30 mg/cm_{geo}², and the values of $\text{Cu}_x\text{Mo}_{100-x}$ were in the range of 0.26–0.48 mg/cm_{geo}².

We used electrochemical analysis to measure the active surface area of the Cu_{100} and $\text{Cu}_x\text{Mo}_{100-x}$ deposits by LSV with a scan rate of 10 mV/s in N_2 -purged 0.5 M NaOH electrolyte at room temperature and atmospheric pressure, as shown in Fig. 2e. In the anodic scan, three types of peaks were observed. Peaks around -0.75 V_{SCE} correspond to the formation of a MoO_2 layer ($\text{Mo} + 4\text{OH}^- \rightarrow \text{MoO}_2 + 2\text{H}_2\text{O} + 4\text{e}^-$), as reported by Mohammed et al. [56]. Obviously, no peaks occurred at this potential in the Cu_{100} deposit, but the intensity of this peak gradually increased in deposits containing Mo and increased with increasing Mo content. For peaks in the range between -0.50 and -0.30 V_{SCE}, the recorded current densities contributed to both of the further oxidation of MoO_2 to MoO_3 ($\text{MoO}_2 + 2\text{OH}^- \rightarrow \text{MoO}_3 + 2\text{H}_2\text{O} + 2\text{e}^-$) [56] and the formation of Cu_2O ($\text{Cu} + \text{OH}^- \rightarrow \text{CuOH} + \text{e}^-$, $2\text{CuOH} \leftrightarrow \text{Cu}_2\text{O} + \text{H}_2\text{O}$) [54]. A further anodic sweep was attributed to the dissolution currents of the Mo and Cu oxides. The ECSAs of Cu_{100} and $\text{Cu}_x\text{Mo}_{100-x}$ were estimated by using charge densities at the anodic peaks

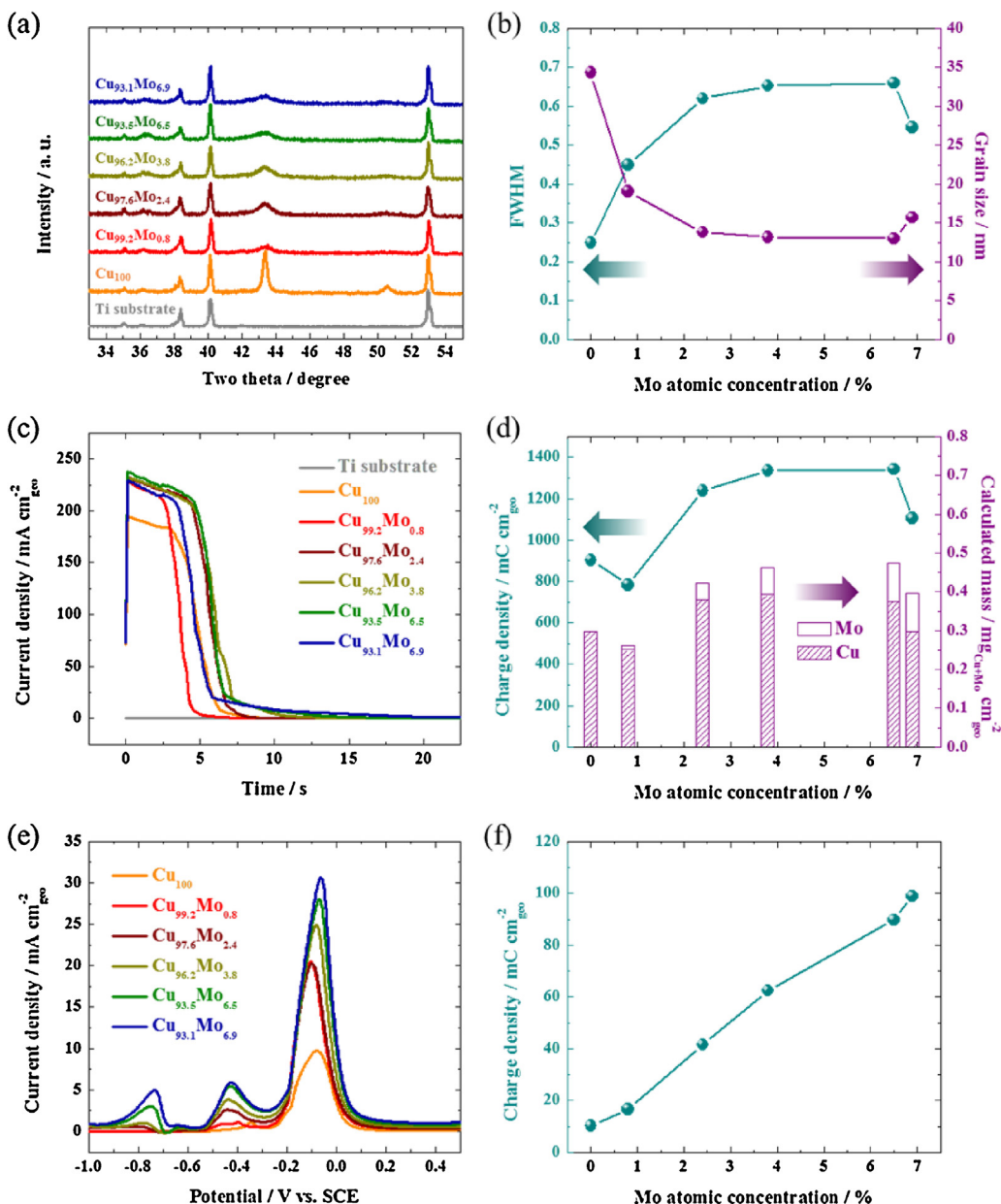


Fig. 2. (a) XRD patterns of Ti substrates, Cu₁₀₀ and Cu_xMo_{100-x}. (b) Calculated FWHM and grain size from XRD as a function of Mo atomic concentration. (c) Current density vs. time curves in 0.5 M H₂SO₄ at 0.5 V_{SCE}. (d) Dissolution charge density and calculated mass depending on Mo atomic concentration. (e) LSVs of Cu₁₀₀ and Cu_xMo_{100-x} in 0.5 M NaOH with a scan rate of 10 mV/s. (f) Calculated charge density of peaks at nearby -0.45 V_{SCE} as a function of Mo atomic concentration.

located at nearby -0.45 V_{SCE}, where reactions for both components (Cu, Mo) occur. As shown in Fig. 2f, the charge densities gradually increased from 10.3 mC/cm_{geo}⁻² to 98.9 mC/cm_{geo}⁻², as the Mo content increased from 0 to 6.9%. This parallels, to some extent, the reduction in the grain size on the incorporation of Mo as shown in Fig. 2b. The smaller Cu grains provide more surfaces vulnerable to the electrochemical oxidation, indicating the enlarged active surface area by addition of Mo.

The catalytic activities of Cu₁₀₀ and Cu_xMo_{100-x} deposits for HER were examined using CV. Fig. 3a shows the first cycle of each sample in 0.5 M H₂SO₄ electrolyte at a scan rate of 50 mV/s. For the Cu₁₀₀ catalyst, the initial HER activity was -9.4 mA/cm_{geo}² at -0.50 V_{RHE}. After adding small amount of Mo (0.8–2.4%), the catalytic activities increased significantly with a current density of between -60.9 and -66.2 mA/cm_{geo}² at -0.50 V_{RHE}, even though the HER exchange current density of Mo is two orders lower than that of Cu [37]. This suggests that a strong synergistic effect

between Cu and Mo occurs, and we will discuss this in detail later. Further current density enhancement was achieved by increasing the Mo content to between 3.8 and 6.9%. The current densities were recorded as -83.4 to -88.9 mA/cm_{geo}² at -0.50 V_{RHE}, reaching saturation in the activity. The redox currents in the range of -0.25 to 0.05 V_{RHE} with Cu_xMo_{100-x}, especially at high Mo content, might originate from the electrochemical reduction of molybdenum oxides during the forward scan and oxidation (or dissolution) of metallic Mo during the backward scan because molybdenum oxide was formed in the Cu_xMo_{100-x} deposits during the co-electrodeposition of CuMo [57].

To understand the reason for the high activity of the Cu_xMo_{100-x} catalysts, we normalized the obtained current densities relative to the calculated mass and charge density (Fig. 2c-f) as demonstrated in Fig. 3b and c, respectively. The normalized activities at -0.50 V_{RHE} from Fig. 3b and c, depending on Mo content, are summarized in Fig. 3d (bars for current density in Fig. 3a, cir-

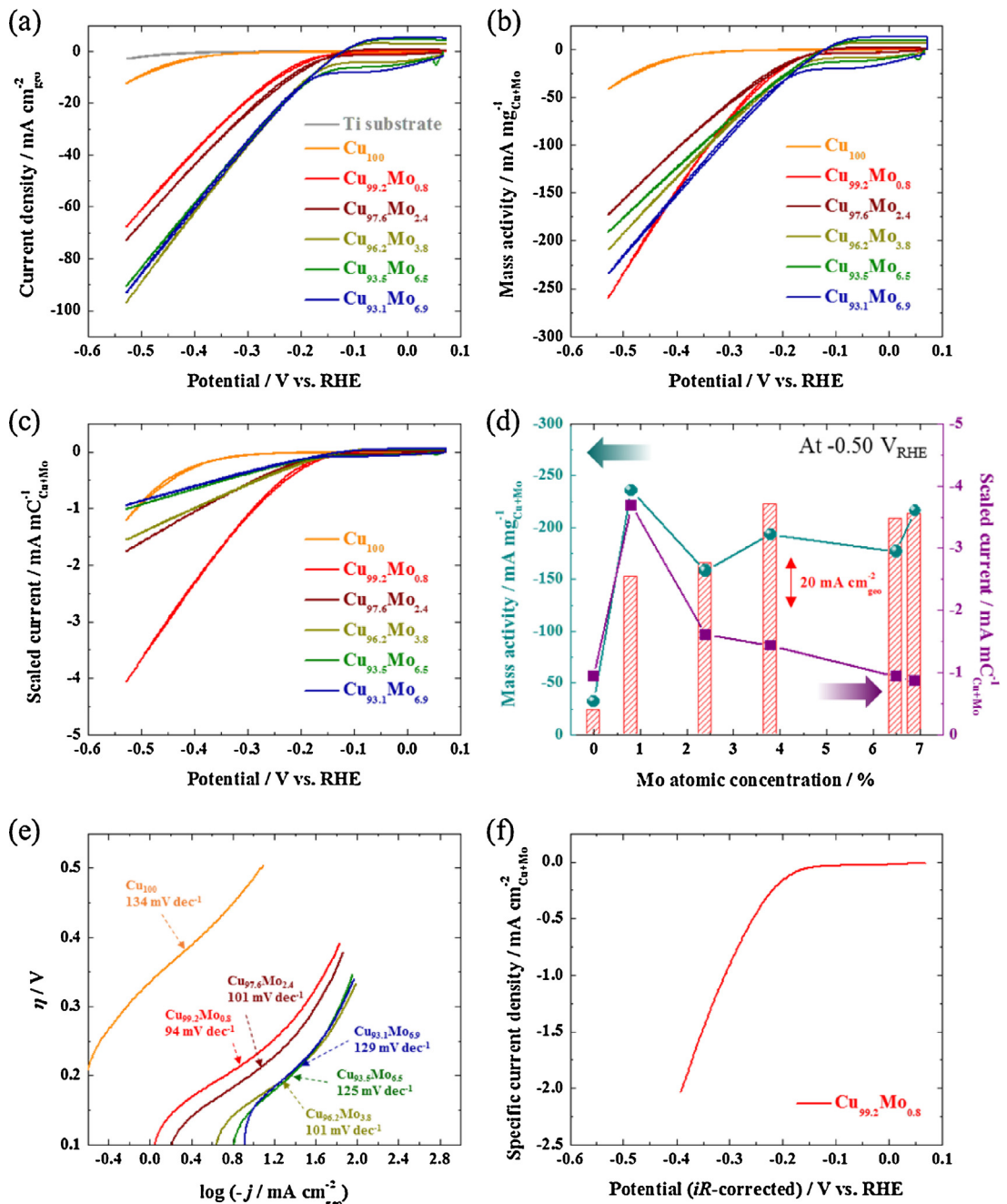


Fig. 3. HER activity measurements by using CVs at scan rate of 50 mV/s based on (a) current density, (b) mass activity and (c) scaled current. (d) Current density, mass activity and scaled current at $-0.50\text{ V}_{\text{RHE}}$ as a function of Mo atomic concentration. (e) Tafel plots of $i\text{R}$ -corrected (a). (f) Specific current density of $\text{Cu}_{99.2}\text{Mo}_{0.8}$.

cles for mass activity in Fig. 3b, and squares for scaled current density in Fig. 3c). Considering the mass, the maximum mass activities of $-233.4\text{ mA/mg}_{\text{Cu+Mo}}$ at $-0.50\text{ V}_{\text{RHE}}$ was obtained with the $\text{Cu}_{99.2}\text{Mo}_{0.8}$ catalyst, 7.4 times larger than Cu_{100} catalyst. However, it should be noted that the $\text{Cu}_{99.2}\text{Mo}_{0.8}$ catalyst did not show a maximum mass activity in the lower overpotential ranges presented in Fig. 3b. At the same overpotential, 0.50 V, the mass activities of the other $\text{Cu}_x\text{Mo}_{100-x}$ catalysts increased by 5.0–6.8 times compared to those of the Cu_{100} catalyst. Meanwhile, the scaled current densities, normalized by the calculated charge densities (which, in turn, relates to the active area) in Fig. 2f, represent the intrinsic activities of Cu_{100} and $\text{Cu}_x\text{Mo}_{100-x}$ catalysts. As shown in Fig. 3c, a substantial increase in the scaled current density was obtained when using the $\text{Cu}_{99.2}\text{Mo}_{0.8}$ catalyst at all potentials. Interestingly, the scaled

current density gradually decreased on increasing the Mo content in the $\text{Cu}_x\text{Mo}_{100-x}$ catalysts. From these results, we concluded that even a very low Mo content had a large effect on the increase in the intrinsic activity. Comparing the geometric current density and normalized current density, the geometric current density of the $\text{Cu}_{96.2}\text{Mo}_{3.8}$ catalyst is the highest, whereas the $\text{Cu}_{99.2}\text{Mo}_{0.8}$ catalyst demonstrated the highest mass activity and scaled current among the all $\text{Cu}_x\text{Mo}_{100-x}$ catalysts.

Fig. 3e shows the Tafel plots for forward scans of $i\text{R}$ -corrected CVs (see Fig. S3 in the Supporting Information), which can be correlated to the HER mechanism. Previously, the HER mechanism in acidic electrolyte has been postulated to comprise three steps [57]. The first step is the Volmer reaction, which is related to the discharge of proton ($\text{H}_3\text{O}^+ + \text{e}^- \rightarrow \text{H}_{\text{ad}} + \text{H}_2\text{O}$,

$b = 2.3RT/\alpha F = 120 \text{ mV}$, $\alpha = 0.5$). Then, two possible steps are proposed: The Heyrovsky ($\text{H}_{\text{ad}} + \text{H}_3\text{O}^+ + \text{e}^- \rightarrow \text{H}_2 + \text{H}_2\text{O}$, $b = 40 \text{ mV}$) and Tafel reactions ($\text{H}_{\text{ad}} + \text{H}_{\text{ad}} \rightarrow \text{H}_2$, $b = 30 \text{ mV}$). The slope of the Tafel plot of the Cu_{100} catalyst in Fig. 3e was 134 mV dec^{-1} , indicating that proton discharge on the surface is the rate determining step. After the addition of a small amount of Mo (0.8%), the slope of the Tafel plot decreased to 94 mV dec^{-1} . For $\text{Cu}_{99.2}\text{Mo}_{0.8}$, the obtained slope of 94 mV dec^{-1} is comparable to those obtained for Cu_2MoS_4 (95 mV dec^{-1}) [58] and Cu-MoS₂ on reduced graphene oxide (90 mV dec^{-1}) [63]. On further increasing of Mo contents, the Tafel slope increased again to 101 mV dec^{-1} – 129 mV dec^{-1} , demonstrating that the rate determining step relates to the Volmer reaction again. The results of Tafel slopes were well matched to the activity trend obtained from the scaled current densities (Fig. 3d).

To estimate the HER activity based on the real surface area, the electrochemical double-layer capacitance of Cu_{100} and $\text{Cu}_x\text{Mo}_{100-x}$ catalysts were measured in $0.5 \text{ M H}_2\text{SO}_4$ electrolyte, as shown in the Supporting Information (Fig. S4). In the potential range of -0.25 to $-0.15 \text{ V}_{\text{SCE}}$, repeated CVs were conducted by varying the scan rate from 0.005 to 0.800 V/s , following a previously reported method [19,20]. Then, $\Delta i/2$ (where $\Delta i = i_{\text{anodic}} - i_{\text{cathodic}}$) at a potential of $-0.20 \text{ V}_{\text{SCE}}$ was plotted against the scan rate (see Fig. S5 in the Supporting Information). For both Cu_{100} and $\text{Cu}_{99.2}\text{Mo}_{0.8}$ catalysts, a linear correlation between $\Delta i/2$ and scan rate was found. The slopes were $0.251 \text{ mF/cm}_{\text{geo}}^2$ for Cu_{100} and $1.663 \text{ mF/cm}_{\text{geo}}^2$ for $\text{Cu}_{99.2}\text{Mo}_{0.8}$, and the obtained values were converted to approximate roughness factors (RFs) with specific double layer capacitances of $50 \mu\text{F/cm}_{\text{Cu}}^2$ for Cu [60] and $27 \mu\text{F/cm}_{\text{Mo}}^2$ for Mo [61]. Based on the RFs, the specific current densities of the $\text{Cu}_{99.2}\text{Mo}_{0.8}$ catalyst are shown in Fig. 3f; furthermore, at an overpotential of 100 mV , the specific current density was $0.033 \text{ mA/cm}_{\text{Cu+Mo}}^2$, higher than those of various transition metal alloys, for example, CoMo (0.004) [19], CoW (0.004) [19], Mo/S (0.013) [19], NiMoFe (0.014) [19], and NiW (0.014) [19], although this value was lower than those of several Ni-based alloys, such as NiMo (0.074) [19] and NiMoCo (0.043) [19]. However, it should be noted that the Ni-based alloys may suffer from dissolution during HER.

XPS analysis was conducted on the $\text{Cu}_{96.2}\text{Mo}_{3.8}$ deposit, which is an intermediate composition of all the $\text{Cu}_x\text{Mo}_{100-x}$ deposits, as shown in Fig. 4. For the Cu 2p3/2 spectra, the binding energy of the $\text{Cu}_{96.2}\text{Mo}_{3.8}$ deposit was determined to be 932.1 eV , which is 0.4 eV lower than that of the Cu_{100} deposit, suggesting that the Cu in CuMo is in an electron-rich state (Fig. 4a). Although the atomic radius of Mo (139 pm) is larger than that of Cu (128 pm), the Cu 2p3/2 spectra of $\text{Cu}_{96.2}\text{Mo}_{3.8}$ indicate an electron-rich state due to the difference in the electronegativity of Cu (1.9) and Mo (1.8). Meanwhile, the electronic structure of Mo was also analyzed from their 3d spectra (Fig. 4b). Compared with metallic Mo (3d3/2 peak at 230.7 eV and 3d5/2 peak at 227.5 eV) [62] the XPS spectra of Mo 3d doublets demonstrated the higher binding energy of $\sim 4.3 \text{ eV}$ (3d3/2 peak at 235.0 eV and 3d5/2 at 231.8 eV), indicating that the oxidation state of Mo is about +5 [62]. This value is close to the oxidation state of Mo_4O_{11} (+5.5) [63], implying that Mo in CuMo exists as, at least in some part, as oxides, and similar oxidized states of the Mo XPS spectra have been observed in Cu_2MoS_4 [58], Cu-MoS₂ on reduced graphene oxide (rGO) [59] and Cu@MoS₂ on multi-walled carbon nanotubes (MWCNTs) [64], which have high catalytic activities for acidic HER. Combined with the scaled current density shown in Fig. 3c and d, the similarity of the electronic structure of $\text{Cu}_x\text{Mo}_{100-x}$ with that of Cu-Mo-S ternary catalysts [58,59,64] might be the reason for the improved HER activity. In addition, the grain size of the $\text{Cu}_x\text{Mo}_{100-x}$ deposits, as shown in Fig. 2b, must be considered. Wang et al. have reported that small MoO₂ nanoparticles ($\sim 10 \text{ nm}$) show enhanced catalytic activity for HER [65]. However, increasing the Mo content increases the Mo surface

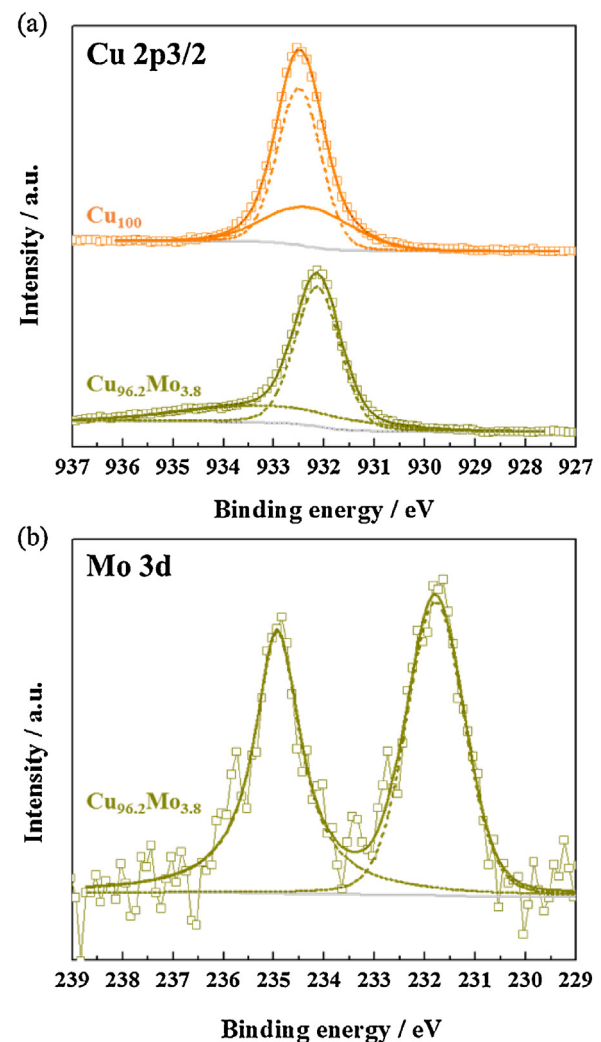


Fig. 4. XPS spectra of Cu_{100} and $\text{Cu}_{96.2}\text{Mo}_{3.8}$ catalysts. (a) Cu 2p3/2 and (b) Mo 3d.

concentration, which has an HER activity two orders of magnitude smaller than that of Cu [37]. Thus, a compromise is required to explain the intrinsic activity of the $\text{Cu}_x\text{Mo}_{100-x}$ catalysts.

To test the stability of the $\text{Cu}_x\text{Mo}_{100-x}$ catalysts, we measured CVs in $0.5 \text{ M H}_2\text{SO}_4$ electrolyte with a scan rate of 50 mV/s (not iR -corrected). Fig. S6a–e demonstrate three selected CV scans of the HER for each sample obtained in the non-divided batch cell; these scans consist of the 1st cycle, an intermediate cycle with a minimum current density, and the 500th cycle. Detailed data concerning the current densities at $-0.50 \text{ V}_{\text{RHE}}$ are summarized in Fig. S6f. For the $\text{Cu}_{99.2}\text{Mo}_{0.8}$ catalyst (Fig. S6a), in the 1st scan, the current density was $-60.9 \text{ mA/cm}_{\text{geo}}^2$ at $-0.50 \text{ V}_{\text{RHE}}$, then showed a further decreasing to $-26.5 \text{ mA/cm}_{\text{geo}}^2$ after the 20th cycle. The reduction in activity may originate from the dissolution of Mo during cycling (the standard reduction potential of Mo is $-0.200 \text{ V}_{\text{NHE}}$), resulting in the disappearance of the positive effects attributed to the presence of Mo, particularly electronic effects, as discussed above. With further cycling, the catalytic activity gradually increased back to $-46.1 \text{ mA/cm}_{\text{geo}}^2$ at the 500th cycle. Similar fluctuations in catalytic activity also occurred with the $\text{Cu}_{97.6}\text{Mo}_{2.4}$ catalyst (Fig. S6b), but the minimum current density was observed after a greater number of cycles (100) due to the higher Mo content. In contrast, for Mo content in the range of 3.8–6.9%, the recorded current densities after 500 cycles at $-0.50 \text{ V}_{\text{RHE}}$ remained stable, maintaining the same current density as that recorded initially (Fig. S6c–e). The first reason for this behavior is the large Mo content, confirmed by

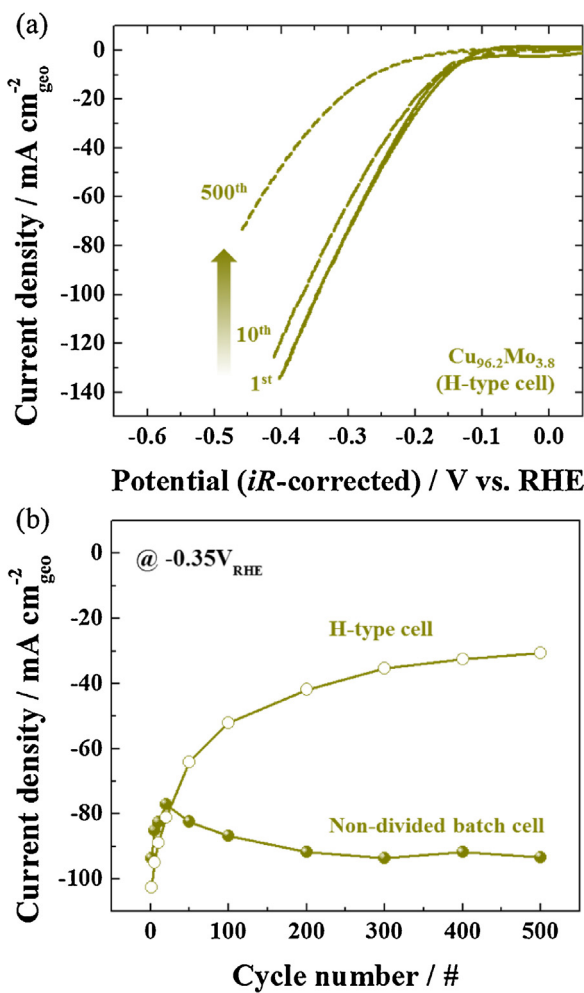


Fig. 5. (a) Selected CV scans of $\text{Cu}_{96.2}\text{Mo}_{3.8}$ (iR-corrected) measured in the H-type cell. (b) Current densities at $-0.35 \text{ V}_{\text{RHE}}$ as a function of cycle number.

the fact that the redox currents in the ranges of -0.20 to $0.05 \text{ V}_{\text{RHE}}$ are still observed after 500 cycles, despite the deterioration with increasing cycle numbers. However, concerning the onset potential of the HER, this explanation is insufficient because the onset potentials after the 1st cycle shifted in the positive direction after 500th cycles, despite the current density at $-0.50 \text{ V}_{\text{RHE}}$ barely changing (Fig. S6c–e). To understand this change, we carried out XPS analysis on the $\text{Cu}_{96.2}\text{Mo}_{3.8}$ catalyst after the 1st, 20th, 100th, and 500th cycles (Fig. S7a). Interestingly, the Pt 4d peak appeared after the 100th cycle, and its intensity increased after the 500th cycle. The calculated Pt surface concentrations are 1.3% at the 100th cycle and 4.4% at the 500th (Fig. S7b). Pt is deposited on the surface of the $\text{Cu}_{96.2}\text{Mo}_{3.8}$ catalyst due to the reduction of Pt ions dissolved from Pt counter electrode during the repeated CVs, and this greatly contributed to the activities after repeated cycles, particularly in the cases of samples with higher Mo contents (Note that samples with higher Mo contents exhibited larger current during CV, therefore generated larger amounts of dissolved Pt at the counter electrode). A similar result in HER enhancement was observed using an Au working electrode and a Pt counter electrode [66].

From the XPS analysis, it was revealed that the stability of $\text{Cu}_x\text{Mo}_{100-x}$ catalysts in the non-divided batch cell was significantly affected by Pt contamination during this acidic HER test with the designated potential range. Thus, the H-type cell containing Nafion membrane was used to avoid the Pt contamination during the repeated CV measurements. Fig. 5a and Fig. S8 demonstrate three selected CV scans of the repeated HER for $\text{Cu}_{96.2}\text{Mo}_{3.8}$

catalyst obtained by using the H-type cell and the non-divided batch cell, respectively. Due to the difference of cell configurations, the obtained potentials were iR-corrected with the solution resistances. The detailed data was summarized in Fig. 5b. With increase of cycle number, the current densities with the H-type cell was gradually decreased due to the dissolution of Mo species as the redox currents in the range of -0.25 to $0.05 \text{ V}_{\text{RHE}}$ became narrowed. For testing a single-cell PEMWE performance using the developed catalyst, CuMo was electrodeposited on CP in $0.05 \text{ M CuSO}_4 + 0.10 \text{ M Na}_2\text{MoO}_4 + 0.25 \text{ M Na}_3\text{C}_6\text{H}_5\text{O}_7$ electrolyte, which was used to fabricate the $\text{Cu}_{96.2}\text{Mo}_{3.8}$ catalyst on a Ti substrate (see Table S1) that exhibited the highest geometric current density. The deposition potential was $-1.0 \text{ V}_{\text{SCE}}$ for 600 s. Fig. 6a and b show the bare CP at low and high magnifications, respectively. After electrodeposition, the surfaces of carbon fibers were mostly covered by CuMo deposits, as shown in Fig. 6c and d. ICPMS analysis indicates that the total metal loading of the paper was $62 \mu\text{g}/\text{cm}^2$ (Cu for $56.3 \mu\text{g}/\text{cm}^2$ and Mo for $5.7 \mu\text{g}/\text{cm}^2$). Based on ICPMS results, we determined that the deposit consists of 93.7% Cu and 6.3% Mo, where the Mo content was greater than that deposited on Ti substrate under the same electrolyte composition. This is very similar to the $\text{Cu}_{93.5}\text{Mo}_{6.5}$ deposit on Ti substrate, which exhibited the saturated mass activity and geometric current density. At high magnification, the morphology of $\text{Cu}_{93.7}\text{Mo}_{6.3}/\text{CP}$ (Fig. 6d) was also very similar to those of $\text{Cu}_{93.5}\text{Mo}_{6.5}/\text{Ti}$ and $\text{Cu}_{93.1}\text{Mo}_{6.9}/\text{Ti}$ (Fig. 1), and this deposited catalyst was further used as the cathode for subsequent PEMWE single cell performance test. To prepare the anode, the electrodeposited IrO_2/CP was prepared following the fabrication procedure reported previously [7]. The mass loading of IrO_2 on CP obtained from ICPMS analysis is $0.10 \text{ mg}/\text{cm}^2$ [7].

Fig. 7a shows the polarization curves of the PEMWE single cell adopting the IrO_2/CP anode and $\text{Cu}_{93.7}\text{Mo}_{6.3}/\text{CP}$ cathode. While using the potentiostatic method described in the experimental section, we found that the cell performance gradually increased from the 1st to 3rd cycle, stabilizing between the 3rd and 12th cycle. This increase in the initial stages of operation has also been observed for single cell operation, as we have reported previously [7]. From the 12th operation, the recorded current density at $1.9 \text{ V}_{\text{cell}}$ was about $0.50 \text{ A}/\text{cm}^2$. It should be noted that despite the current density decay by Mo dissolution in repeated CVs, the single cell exhibited stable performances since the cathodic overpotential prevented dissolution of the CuMo catalysts. For comparison, the current densities of PEMWE operation at $1.9 \text{ V}_{\text{cell}}$ published in the recent literatures are summarized in Fig. 7b, and the operation conditions for each point are provided in the Supporting Information (Table S2). Recently, noble metals or their oxides (Pt or Pt/C, and Ir or Ir oxide) have been used for both cathode and anode. The reported current densities using the Pt cathode were in the range of 1.82 – $2.87 \text{ A}/\text{cm}^2$ at 1.9 V , 3.6–5.7 times higher than that of our PEMWE using a non-noble metal cathode. In contrast, the mass activity of our non-noble metal PEMWE is $3.4 \text{ A}/\text{mg}_{\text{metal}}$, a larger value than those reported in the literature, despite the use of a non-noble metal, indicating the advantages of using electrodeposition to prepare the catalyst with respect to mass loading (Fig. 7c). However, our previously reported PEMWE [7] has better performance, $4.6 \text{ A}/\text{mg}_{\text{metal}}$, due to the use of a Pt cathode and electrodeposited IrO_2 anode with low mass loading. Interestingly, the catalyst cost-activity relationship calculated using recent metal prices (March 2016) [67] indicates a 2.2–10.8 times higher cost-activity than those of previously reported catalysts (Fig. 7d), suggesting the suitability of the non-noble cathode for PEMWE operation. In conclusion, as far as we know, this study is the first implementation of the non-noble cathode for single cell operation of a PEMWE. However, further investigation is required to improve the performance of the PEMWE. We believe that improvement can be achieved by increasing the catalyst loading using nanostructured supports with

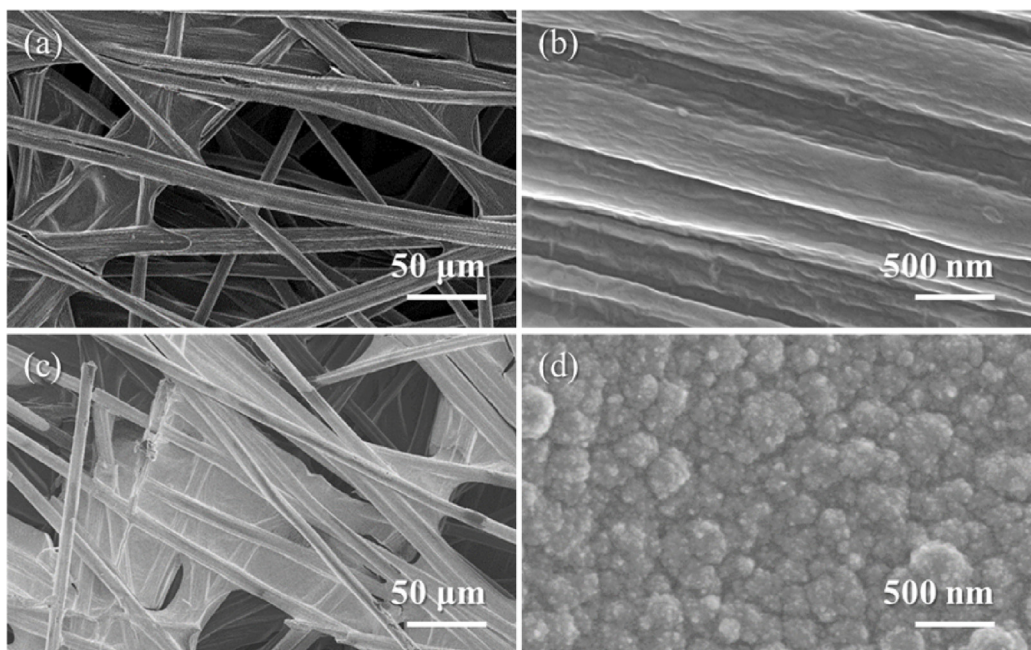


Fig. 6. (a) FESEM image of bare carbon paper. (b) Expanded image of (a). (c) FESEM image of Cu_{93.7}Mo_{6.3} deposited carbon paper. (d) Expanded image of (c).

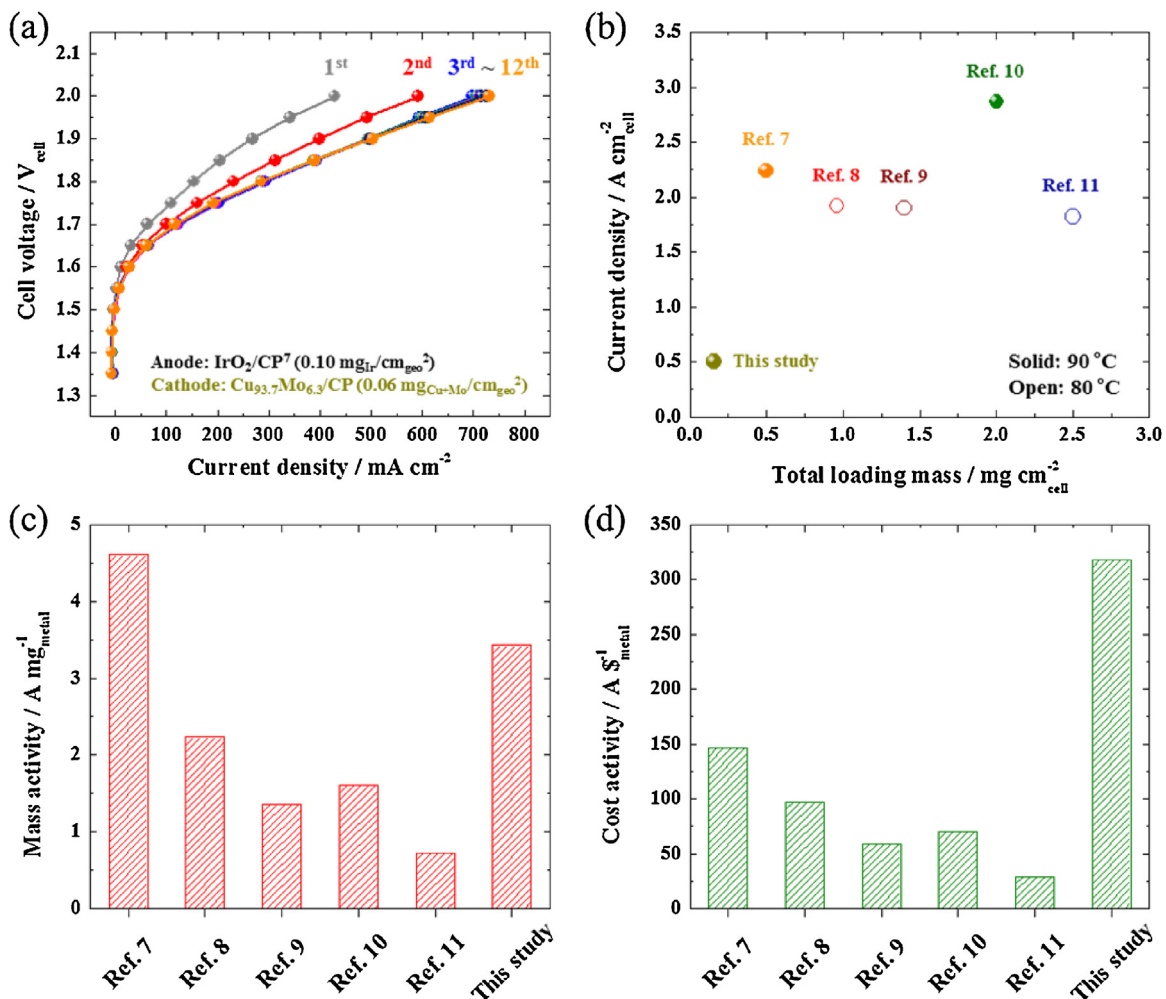


Fig. 7. (a) i-V curves of PEMWE operation employing IrO₂/CP anode and Cu_{93.7}Mo_{6.3}/CP cathode. (b) Current density at cell voltage of 1.9 V_{cell} as a function of total loading mass of catalysts. (c) Mass activity comparison. (d) Cost activity comparison.

ultra-high surface areas. In addition, it should be noted that the cost of the CuMo cathode in the case of high mass loading mass is negligible compared to that of the currently used Pt noble metal cathode.

4. Conclusions

$\text{Cu}_x\text{Mo}_{100-x}$ was deposited by electrodeposition for use as an electrocatalyst for hydrogen production in an acidic electrolyte. The morphologies and atomic concentrations of $\text{Cu}_x\text{Mo}_{100-x}$ deposits were controlled by varying the electrolyte composition. The material properties were carefully characterized by microscopic, crystallographic, electrochemical, and spectroscopic techniques. In addition to the changes in the electronic structure of Mo, the co-deposition of CuMo resulted in the formation of nanocrystalline $\text{Cu}_x\text{Mo}_{100-x}$ grains with high surface area, confirmed by the increase in the dissolution charges and broader peaks in the XRD patterns. As a result, the intrinsic activity of CuMo catalyst was increased by maximum 7.4 times higher than that of Cu_{100} catalyst at $-0.50 \text{ V}_{\text{RHE}}$. The stability of the catalyst was also investigated in terms of Mo dissolution. To examine the practicality of these catalysts, one of the $\text{Cu}_x\text{Mo}_{100-x}$ samples was deposited on carbon paper as an HER electrode for single-cell PEMWE operation, using an electrodeposited IrO_2 anode. The cost-activity relationship, based on the metallic mass activity, was 2.2–10.8 times greater than those of recently reported PEMWEs using noble metal catalysts.

Acknowledgments

This research was supported by the KIST Institutional Program (2E24841). This work was supported by the National Research Foundation of Korea (NRF) Grant funded by the Korean Government MSIP (2016M3A7B4909369) and MOE (2016R1D1A1B03931963).

Appendix A. Supplementary data

Supplementary data associated with this article can be found, in the online version, at <http://dx.doi.org/10.1016/j.apcatb.2017.01.074>.

References

- [1] J.A. Turner, Science 305 (2004) 972–974.
- [2] M.K. Debe, Nature 486 (2012) 43–51.
- [3] J.H. Williams, A. DeBenedictis, R. Ghanadan, A. Mahone, J. Moore, W.R. Morrow, S. Price, M.S. Torn, Science 335 (2012) 53–59.
- [4] K. Christopher, R. Dimitrios, Energy Environ. Sci. 5 (2012) 6640–6651.
- [5] L. Xiao, S. Zhang, J. Pan, C. Yang, M. He, L. Zhuang, J. Lu, Energy Environ. Sci. 5 (2012) 7869–7871.
- [6] M. Carmo, D.L. Fritz, J. Mergel, D. Stoltzen, Int. J. Hydrogen Energy 38 (2013) 4901–4934.
- [7] B.-S. Lee, S.H. Ahn, H.-Y. Park, I. Choi, S.J. Yoo, H.-J. Kim, D. Henkensmeier, J.Y. Kim, S. Park, S.W. Nam, K.-Y. Lee, J.H. Jang, Appl. Catal. B Environ. 179 (2015) 285–291.
- [8] C. Rozain, E. Mayousse, N. Guillet, P. Millet, Appl. Catal. B Environ. 182 (2016) 153–160.
- [9] H.-S. Oh, H.N. Nong, T. Reier, M. Gliech, P. Strasser, Chem. Sci. 6 (2015) 3321–3328.
- [10] S. Siracusano, N.V. Dijk, E. Payne-Johnson, V. Baglio, A.S. Arico, Appl. Catal. B Environ. 164 (2015) 488–495.
- [11] L. Ma, S. Sui, Y. Zhai, Int. J. Hydrogen Energy 34 (2009) 678–684.
- [12] Y. Leng, G. Chen, A.J. Mendoza, T.B. Tighe, M.A. Hickner, C.-Y. Wang, J. Am. Chem. Soc. 134 (2012) 9054–9057.
- [13] S.H. Ahn, S.J. Yoo, H.-J. Kim, D. Henkensmeier, S.W. Nam, S.-K. Kim, J.H. Jang, Appl. Catal. B Environ. 180 (2016) 674–679.
- [14] S.H. Ahn, B.-S. Lee, I. Choi, S.J. Yoo, H.-J. Kim, E.A. Cho, D. Henkensmeier, S.W. Nam, S.-K. Kim, J.H. Jang, Appl. Catal. B Environ. 154–155 (2014) 197–205.
- [15] X. Wu, K. Scott, J. Power Sources 214 (2012) 124–129.
- [16] X. Wu, K. Scott, Int. J. Hydrogen Energy 38 (2013) 3123–3129.
- [17] C.C. Pavel, F. Cecconi, C. Emiliani, S. Santuccioli, A. Scaffidi, S. Catanorchi, M. Comotti, Angew. Chem. 126 (2014) 1402–1405.
- [18] D.V. Esposito, S.T. Hunt, A.L. Stottlemyer, K.D. Dobson, B.E. McCandless, R.W. Birkmire, J.G. Chen, Angew. Chem. Int. Ed. 49 (2010) 9859–9862.
- [19] C.C.L. McCrory, S. Jung, I.M. Ferrer, S.M. Chatman, J.C. Peter, T.F. Jaramillo, J. Am. Chem. Soc. 137 (2015) 4347–4357.
- [20] C.C.L. McCrory, S. Jung, J.C. Peters, T.F. Jaramillo, J. Am. Chem. Soc. 135 (2013) 16977–16987.
- [21] T. Reier, M. Oezaslan, P. Strasser, ACS Catal. 2 (2012) 1765–1772.
- [22] E.A. Paoli, F. Masini, R. Frydendal, D. Deiana, C. Schlaup, M. Malizia, T.W. Hansen, S. Horsch, I.E.L. Stephens, I. Chorkendorff, Chem. Sci. 6 (2015) 190–196.
- [23] N. Danilovic, R. Subbaraman, K.-C. Chang, S.H. Chang, Y.J. Kang, J. Snyder, A.P. Paulikas, D. Strmenik, Y.-T. Kim, D. Myers, V.R. Stamenkovic, N.M. Markovic, J. Phys. Chem. Lett. 5 (2014) 2474–2478.
- [24] I.C. Man, H.-Y. Su, F. Calle-Vallejo, H.A. Hansen, J.I. Martinez, N.G. Inoglu, J. Kitchin, T.F. Jaramillo, J.K. Norskov, J. Rossmeisl, ChemCatChem 3 (2011) 1159–1165.
- [25] R. Frydendal, E.A. Paoli, B.P. Knudsen, B. Wickman, P. Malacrida, I.E.L. Stephens, I. Chorkendorff, ChemElectroChem 1 (2014) 2075–2081.
- [26] E. Antolini, ACS Catal. 4 (2014) 1426–1440.
- [27] J.Y. Kim, J. Choi, H.Y. Kim, E. Hwang, H.-J. Kim, S.H. Ahn, S.-K. Kim, Appl. Surf. Sci. 359 (2015) 227–235.
- [28] S.H. Ahn, H. Tan, M. Haensch, Y. Liu, L.A. Bendersky, T.P. Moffat, Energy Environ. Sci. 8 (2015) 3557–3562.
- [29] N.B. Halck, V. Petrykin, P. Krtl, J. Rossmeisl, J. Phys. Chem. Chem. Phys. 16 (2014) 13682–13688.
- [30] S.J. Trasatti, Electroanal. Chem. 39 (1972) 163–184.
- [31] W. Sheng, H.A. Gasteiger, Y. Shao-Horn, J. Electrochem. Soc. 157 (2010) B1529–B1536.
- [32] J. Durst, A. Siebel, C. Simon, F. Hasche, J. Herranz, H.A. Gasteiger, Energy Environ. Sci. 7 (2014) 2255–2260.
- [33] Y. Jiao, Y. Zheng, M. Jaroniec, S.Z. Qiao, Chem. Soc. Rev. 44 (2015) 2060–2086.
- [34] D.V. Esposito, S.T. Hunt, Y.C. Kimmel, J.G. Chen, J. Am. Chem. Soc. 134 (2012) 3025–3033.
- [35] J. Greeley, M. Mavrikakis, Nat. Mater. 3 (2004) 810–815.
- [36] J. Greeley, T.F. Jaramillo, J. Bonde, I. Chorkendorff, J.K. Norskov, Nat. Mater. 5 (2006) 909–913.
- [37] J.K. Norskov, T. Bligaard, A. Logadottir, J.R. Kitchin, J.G. Chen, S. Pandelov, U. Stimming, J. Electrochem. Soc. 152 (2005) J23–J26.
- [38] E. Navarro-Flores, Z. Chong, S. Omanovic, J. Mol. Catal. 226 (2005) 179–197.
- [39] G. Lu, P. Evans, G. Zangari, J. Electrochem. Soc. 150 (2004) A551–A557.
- [40] J.G. Highfield, E. Claude, K. Oguro, Electrochim. Acta 44 (1999) 2805–2814.
- [41] J. Deng, P. Ren, D. Deng, X. Bao, Angew. Chem. Int. Ed. 54 (2015) 2100–2104.
- [42] W.A. Badawy, H. Nady, M. Negem, Int. J. Hydrogen Energy 39 (2014) 10824–10832.
- [43] A. Belanger, A.K. Vijh, Surf. Coat. Technol. 28 (1986) 93–111.
- [44] D.Y. Chung, J.W. Han, D.-H. Lim, J.-H. Jo, S.J. Yoo, H. Lee, Y.-E. Sung, Nanoscale 7 (2015) 5157–5163.
- [45] E.J. Popczun, J.R. McKone, C.G. Read, A.J. Biacchi, A.M. Wiltrot, N.S. Lewis, R.E. Schaak, J. Am. Chem. Soc. 135 (2013) 9267–9270.
- [46] W.-F. Chen, K. Sasaki, C. Ma, A.I. Frenkel, N. Marinovic, J.T. Muckerman, Y. Zhu, R.R. Adzic, Angew. Chem. Int. Ed. 51 (2012) 6131–6135.
- [47] H. Vrubel, D. Merki, X. Hu, Energy Environ. Sci. 5 (2012) 6136–6144.
- [48] W.A. Badawy, H.E. Feky, N.H. Helal, H.H. Mohammed, J. Power Sources 271 (2014) 480–488.
- [49] X. Dai, Z. Li, K. Du, H. Sun, Y. Yang, X. Zhang, X. Ma, J. Wang, Electrochim. Acta 171 (2015) 72–80.
- [50] D. Voiry, H. Yamaguchi, J. Li, R. Silva, D.C.B. Alves, T. Fujita, M. Chen, T. Asefa, V.B. Shenoy, G. Eda, M. Chhowalla, Nat. Mater. 12 (2013) 850–855.
- [51] Z. Wu, B. Fang, A. Bonakdarpour, A. Sun, D.P. Wilkinson, Appl. Catal. B Environ. 125 (2012) 59–66.
- [52] J.M. Velazquez, F.H. Saadi, A.P. Pieterick, J.M. Spurgeon, M.P. Soriaga, B.S. Brunschwig, N.S. Lewis, J. Electroanal. Chem. 716 (2014) 45–48.
- [53] N. Takeno, Atlas of Eh-pH diagrams.
- [54] S.M.A.E. Haleem, B.G. Ateya, J. Electroanal. Chem. 117 (1981) 309–319.
- [55] S.H. Ahn, H.-Y. Park, I. Choi, S.J. Yoo, S.J. Hwang, H.-J. Kim, E.A. Cho, C.W. Yoon, H. Park, H. Son, J.M. Hernandez, S.W. Nam, T.-H. Lim, S.-K. Kim, J.H. Jang, Int. J. Hydrogen Energy 38 (2013) 13493–13501.
- [56] W.A. Badawy, H.E. Feky, N.H. Helal, H.H. Mohammed, Int. J. Hydrogen Energy 38 (2013) 9625–9632.
- [57] B.E. Conway, B.V. Tilak, Electrochim. Acta 47 (2002) 3571–3594.
- [58] P.D. Tran, M. Nguyen, S.S. Pramana, A. Bhattacharjee, S.Y. Chiam, J. Fize, M.J. Field, V. Artero, L.H. Wong, J. Loo, J. Barber, Energy Environ. Sci. 5 (2012) 8912–8916.
- [59] F. Li, L. Zhang, J. Li, X. Lin, X. Li, Y. Fang, J. Huang, W. Li, M. Tian, J. Jin, R.J. Li, Power Sources 292 (2015) 15–22.
- [60] Y. Lu, H. Xu, J. Wang, X. Kong, Electrochim. Acta 54 (2009) 3972–3978.
- [61] W.A. Badawy, A.G. Gad-allah, H.A.A. El-rahman, M.M. Abouromia, Surf. Coat. Technol. 27 (1986) 187–196.
- [62] K.M. Yousif, B.E. Smith, C. Jaynes, J. Mater. Sci. 31 (1996) 185–191.
- [63] T.H. Fleisch, G.J. Mains, J. Chem. Phys. 76 (1982) 780–786.
- [64] F. Li, J. Li, X. Lin, X. Li, Y. Fang, L. Jiao, X. An, Y. Fu, J. Jin, R. Li, J. Power Sources 300 (2015) 301–308.
- [65] X. Li, Y. Jiang, L. Jia, C. Wang, J. Power Sources 304 (2016) 146–154.
- [66] B.L. Abrams, P.C.K. Vesborg, J.L. Bonde, T.F. Jaramillo, I. Chorkendorff, J. Electrochem. Soc. 156 (2009) B273–B282.
- [67] London Metal Exchange Home Page, 2017, <http://www.lme.com> (Accessed 2 April 2016).